

# Partially Supervised Oil-Slick Detection by SAR Imagery Using Kernel Expansion

Grégoire Mercier, *Member, IEEE*, and Fanny Girard-Ardhuin, *Member, IEEE*

**Abstract**—Spaceborne synthetic aperture radar (SAR) is well adapted to detect ocean pollution independently from daily or weather conditions. In fact, oil slicks have a specific impact on ocean wave spectra. Initial wave spectra may be characterized by three kinds of waves, namely big, medium, and small, which correspond physically to gravity and gravity-capillary waves. The increase of viscosity, due to the presence of oil damps gravity-capillary waves. This induces not only a damping of the backscattering to the sensor but also a damping of the energy of the wave spectra. Thus, local segmentation of wave spectra may be achieved by the segmentation of a multiscale decomposition of the original SAR image. In this paper, a semisupervised oil-slick detection is proposed by using a kernel-based abnormal detection into the wavelet decomposition of a SAR image. It performs accurate detection with no consideration to signal stationarity nor to the presence of strong backscatters (such as a ship). The algorithm has been applied on ENVISAT Advanced SAR images. It yields accurate segmentation results even for small slicks, with a very limited number of false alarms.

**Index Terms**—Image analysis, oil spill, satellite applications, sea surface, synthetic aperture radar, water pollution.

## I. INTRODUCTION

THE OCEANIC sea surface is complex and is often governed by nonlinear dynamic systems. Surface waves, which are found in the ocean, range from the millimeter scale to hundreds of meters. By considering an infinite sea surface, the wind induces capillary waves by friction. Capillary waves cannot propagate without wind excitation. But, they transfer their energy to waves with a longer wavelength until they reach an equilibrium that depends on the wind. In addition, gravity waves transfer their energy to gravity-capillary waves. Several models have been proposed to characterize the sea-surface spectrum with an accuracy that depends on the wavelength bandwidth. Those models integrate not only the wind but also the current, atmospheric pressure, and so on. An interesting comparison of some models may be found in [1] in the context

Manuscript received September 30, 2005; revised February 14, 2006. This work was supported by the RITMER program of the French Ministry of Research under the name DetecSuiv, conducted with SAS ActiMar and supported in part by the MARS AIS program of the EU.

G. Mercier is with the GET/Ecole Nationale Supérieure des Télécommunications de Bretagne (ENST Bretagne), ITI Department, CNRS UMR 2872 TAMCIC, TIME team, CS 83818, 29238 Brest Cedex, France (e-mail: gregoire.mercier@enst-bretagne.fr).

F. Girard-Ardhuin is with the Institut Français de Recherche pour l'Exploitation de la MER (IFREMER) DOPS/LOS, 29280 Plouzané, France, and also with the Centre National d'Études Spatiales (CNES), 75001 Paris, France (e-mail: Fanny.Ardhuin@ifremer.fr).

Digital Object Identifier 10.1109/TGRS.2006.881078

of synthetic aperture radar (SAR) imagery. On the one hand, capillary waves are generated by friction, more specifically by friction velocity, related to wind speed and surface properties, which die down when the friction decreases. On the other hand, gravity waves are generated indirectly by sea spectrum energy spreading and propagating over long distances far from their origins.

In fact, backscattering phenomena are directed by gravity-capillary waves (due to the wavelength of electromagnetic waves), while typical SAR systems are sensitive to gravity waves (due to their resolution).

A viscous area is seen smoother than a clean sea surface since small wave generation and propagation is reduced by the viscosity of a slick. From the SAR sensor point of view, a slick is characterized by a lack of backscattered energy and then is restituted through a dark area [2]. According to the Bragg phenomenon, the backscattering process is mostly due to surface roughness. That is why many slick-detection algorithms are based on a thresholding technique [3]–[5]. Nevertheless, this process is not efficient, as slick measurement is sensitive to many parameters (see Section II). Moreover, a radiometric point of view shows some limitations since wave slopes that are not oriented to the sensor are restituted with a lower radiometry that may be confused with small slicks. That is why most slick-detection strategies include a postprocessing stage to remove small slicks through geometrical, morphological, or contextual criteria [6]–[8].

In order to develop a slick-detection scheme in an operational context, the strategy is based on the segmentation of the shape of the local sea-surface wave spectrum. This segmentation is achieved by a kernel expansion that allows to be used with synergistic data. Moreover, the margin maximization is implemented through an abnormal detection technique in order to characterize the normal sea state only (which is then calibrated to the sensor and sea state), while viscous areas are being detected as abnormal observation, if any.

This paper is organized as follows. Section II focuses on the slick measurement through SAR data and outlines the main parameters that are to be taken into consideration in an operational framework. Section III presents the multiscale strategy that allows adding to the initial SAR observation a local sea-surface wave-spectrum point of view. In Section IV, abnormal detection is defined through support vectors (Section IV-A), while Section IV-B focuses on the kernel definition that allows to perform an abnormal detection in the sense of slick detection. Section V shows some typical examples with Environmental Satellite (ENVISAT) Advanced SAR (ASAR) data, and Section VI concludes.

## II. SLICK MEASUREMENT

Benjamin Franklin was among the first modern scientist to be interested in the applications of wave damping by surface slicks [9]. A slick at the ocean surface damps gravity-capillary waves, as explained by Marangoni's theory [10], which is detailed in [11]–[15]. Wave damping is due to the decrease in the surface stress, which is associated with film elasticity, and also to the slick nature, density, and surface viscosity.

Radar is sensitive to surface roughness, which is linked by gravity-capillary waves and is damped by slicks. The radar backscattering level is decreased by the presence of a slick, which appears as a dark patch with weak backscattering in comparison with the surrounding regions.

From a synthesis of previous experimental studies, the best approach to take in detecting slicks is to consider a function of several parameters such as radar configuration, slick nature (natural slick or oil spill), and meteorological and oceanic conditions [16].

- 1) *Wavelength*: Each radar frequency band responds differently, according to wind speed and slick nature [14], [15], [17]–[19]. Several experimental multifrequency studies have shown the greatest contrast with the C-, X-, and Ku-bands by pouring artificial slicks; these results have been confirmed with numerical simulations [20].

The C-band frequency seems to be the most suitable frequency, allowing strong contrasts to be measured up to a wind speed of about  $10\text{--}14\text{ m} \cdot \text{s}^{-1}$  [18].

- 2) *Polarization*: The choice of polarization depends on radar frequency and wind speed. Some experiments have shown that there is no real difference between the HH and VV polarizations for a slick study [21]. However, VV polarization seems to be the most suitable for the C-band, which is notably with strong winds [22], [23].
- 3) *Incidence angle*: The reflection mode of the incident electromagnetic wave is a function of the incidence angle. There are two backscattering mechanisms: a Kirchhoff, for a  $0^\circ$  to  $15^\circ$  incidence angle, and the Bragg reflection, for a  $20^\circ$  to  $70^\circ$  incidence angle. The latter allows observation via the Bragg resonance with gravity-capillary waves that are highly damped by surface films. According to wind constraints and radar frequency, the most suitable incidence angle is from  $20^\circ$  to  $45^\circ$ .
- 4) *Nature of the slick*: Backscatter damping is a function of the slick nature and of the slick properties of viscosity and elasticity [12], [13]. Wave damping is more important for oil spills than for natural slicks in the C-, X-, and Ku-bands [17], whereas natural slicks cause stronger damping with the L-band at low speed [19]. Thus, the use of multifrequency radar measurements may play a role in determining slick nature.
- 5) *Influence of meteorological and oceanic conditions*: The wind is the most important parameter in slick SAR imaging. Efficient radar detection of surface films at the C-band frequency requires a wind speed from  $2\text{--}3$  to  $10\text{--}14\text{ m} \cdot \text{s}^{-1}$  [12], [22]. At lower wind speed, the surface roughness is not uniform, and the calmer areas look like oil spills. At higher wind speeds (up to  $10\text{--}14\text{ m} \cdot \text{s}^{-1}$ ),

backscattering remains high in the slick, and then, contrast decreases. Some conditions produce similar features as oil spills on radar images (look-alike). For example, weak backscatter areas exist over weak wind regions, like in the lee of an island. Some other conditions, like oceanic internal waves, quickly distort slicks that become less dense, thus less easy to detect.

## III. MULTISCALE STRATEGY

*A priori*, the proposed multiscale strategy, which is implemented to detect oil slicks, may be justified by several concepts mentioned above.

- 1) The SAR sensor is only sensitive to surface roughness (at a centimeter scale), which is modulated by larger scale phenomena that induce shades of texture.
- 2) The increase of viscosity, which is due to the presence of an oil slick on the sea surface, affects the sea-surface wave spectrum shape.
- 3) The oil slicks induce dark areas on the SAR images under certain conditions such as limited wind (i.e., under  $10\text{--}14\text{ m} \cdot \text{s}^{-1}$ ).

The wavelet transform is an appropriate tool for the local analysis of the sea wave spectrum. Two parameters are necessary to characterize a multiscale representation: time and scale. Scale defines a concept linked with a frequency characterization that is time dependent.

A multiscale transform is not a multiresolution transform since it does not include decimation steps; it may be implemented in several forms. When a signal is decomposed into a multiscale representation, the details of each band of the decomposition are represented in a progressive manner (that is to say, the bound frequency  $\omega_{\max}$  of the Fourier spectrum is increasing). On the contrary, when using a multiresolution tool, detail levels remain the same in each band (Fourier spectra are of the same bandwidth), but the sampling is modified. In this paper, we focus on the multiscale decomposition with a wavelet transform that is shift invariant. Hence, details and texture have the same signature whatever is their location.

Many shapes may be found in mother wavelets (but they are subject to admissibility conditions [24]), and the choice of the best wavelet remains an open question, which depends on the application. The wavelet transform is defined in order to detect sharp variations and also to characterize the local shape of a signal at different scale. Then, the mother wavelet is defined as the first derivative of a smoothing function  $\theta(x)$  (i.e., this function is the impulse response of a low-pass filter)

$$\psi(x) = \frac{d\theta(x)}{dx}.$$

This constraint has been proposed by Mallat and Zhong in order to build a wavelet frame that acts as a multiscale differential operator [25]. According to this point of view, the wavelet coefficients are proportional to the components of the gradient of the signal smoothed by  $\theta(\cdot)$  at a scale  $2^j$  [which is equivalent to a smoothing function  $\theta_j(x) = \theta(x/2^j)$ ]. With such a multiscale differential operator, each singularity of the signal is detected by following the modulus maxima of the wavelet

coefficients toward finer scales. Moreover, it has been shown that, if the signal has a band-limited Fourier transform and if the wavelet has a compact support, then the wavelet modulus maxima define a complete and stable signal representation [26].

In this paper, this wavelet representation is used for analysis only. In two-dimensional (2-D), the multiscale differential operator is defined in the same way as the Canny edge detector, which detects points of sharp variation by calculating the modulus of the gradient vector of the signal. Then, two 1-D mother wavelets are defined as

$$\psi^x(x) = \frac{d\theta(x)}{dx}, \quad \psi^y(y) = \frac{d\theta(y)}{dy}$$

where the superscripts “ $x$ ” and “ $y$ ” stand for the vertical and horizontal decompositions. That means that, in such a wavelet decomposition, there is no need for a diagonal decomposition, as it is usually the case for multiresolution analysis [27].

The decomposition of an image  $I$  [where the pixel value at position  $(x, y)$  is denoted  $I(x, y)$ ] is achieved by a convolution with a smoothing function  $\theta(x, y) = \theta(x)\theta(y)$  that yields the smoothed image denoted by  $I_1^{\text{low}}$ . Two convolutions with the wavelets  $\psi^x(x)$  and  $\psi^y(y)$  are also applied on images  $I$  to yield gradient images at scale  $\ell = 1$ , which is denoted by  $W_1^x I(x, y) = I *^x \psi^x(x) = (d/dx)(I *^x \theta(x))$  and  $W_1^y I(x, y) = I *^y \psi^y(y) = (d/dy)(I *^y \theta(y))$ .  $*^x$  (resp.  $*^y$ ) stands for the convolution on  $x$  (resp.  $y$ ) only. At coarser level, the decomposition is applied on the smoothed image  $I_\ell^{\text{low}}$ , so that the overall decomposition up to a scale  $L$  may be denoted as the set of  $2L + 1$  images

$$I \longrightarrow \begin{cases} I_L^{\text{low}} = I * \theta\left(\frac{x}{2^{(L-1)}}, \frac{y}{2^{(L-1)}}\right) \\ W_\ell^x I = \frac{d}{dx} \left( I *^x \theta\left(\frac{x}{2^\ell}\right) \right) \\ W_\ell^y I = \frac{d}{dy} \left( I *^y \theta\left(\frac{y}{2^\ell}\right) \right) \end{cases} \quad (1)$$

with  $0 \leq \ell < L$  (see Fig. 1).

In order to analyze the observations as locally as possible, the scale function  $\theta(\cdot)$  was chosen as short as possible, and its Fourier transform is a cubic spline. The low-pass and high-pass coefficients are then defined (in  $z$  transform) by

$$\begin{aligned} H(z) &= (z^{-1} + 3 + 3z + z^2)/8 \\ G(z) &= -2 + 2z. \end{aligned} \quad (2)$$

The high-pass filter corresponds to the discrete approximation of the derivative operator. When applied to SAR images, it is not necessary to use more than two or three levels since  $I_{L=2}^{\text{low}}$  or  $I_{L=3}^{\text{low}}$  contains details at the swell scale, which is enough for our application.

#### IV. KERNEL-BASED ANOMALY DETECTION

We consider the problem of finding oil slick from a SAR image as a detection problem instead of a classification one. In fact, a SAR image of the sea surface may not contain any slick. If any, a slick may not be statistically representative. So,

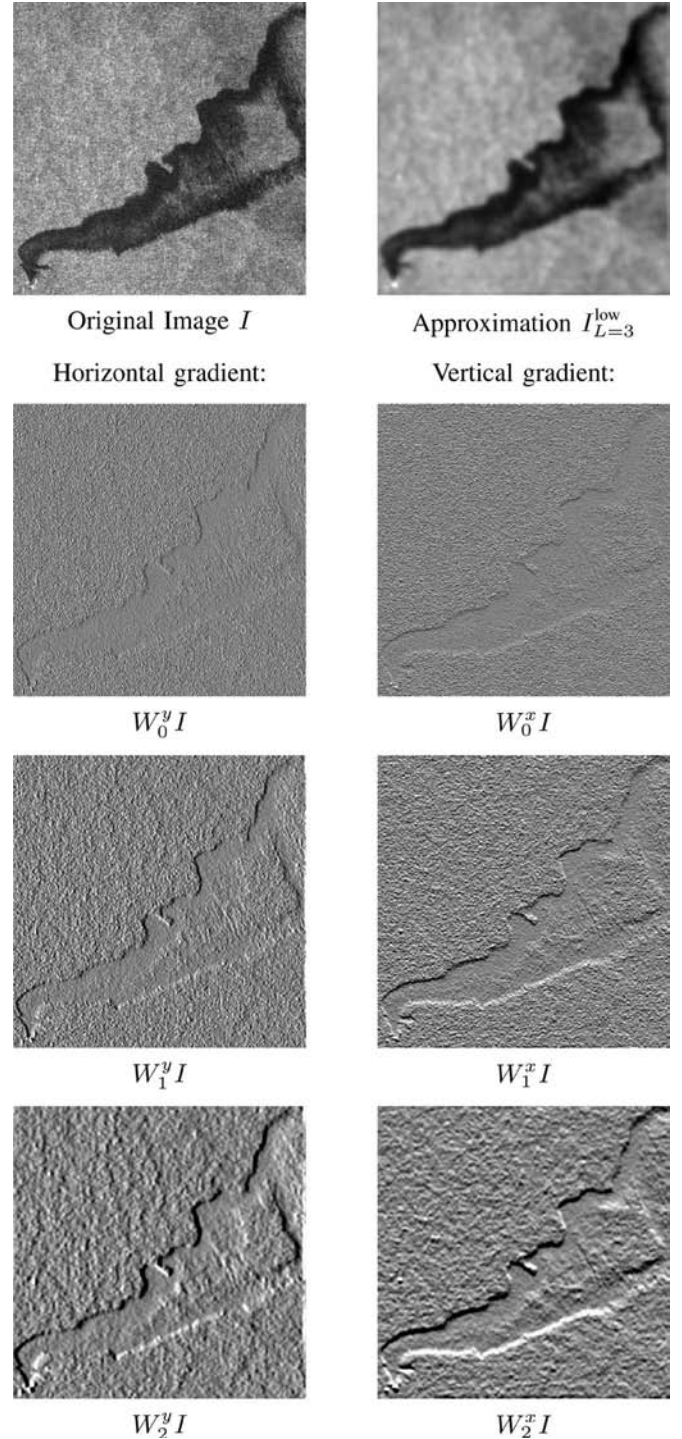


Fig. 1. Multiscale decomposition of a SAR image. Lossless characterization of the initial information is performed through images of wavelet coefficients. Images  $W_\ell^x I$  (respectively,  $W_\ell^y I$ ) contain the vertical (respectively, horizontal) detections of sharp variation and the characterization of local texture at scale  $\ell$  ( $0 \leq \ell < 3$ ). The image  $I_{L=3}^{\text{low}}$  is the coarse approximation of  $I$  at level 3.

a classification approach may have limited performances, and the results would be very sensitive to the image content.

##### A. Support Vectors for Abnormal Detection

Let us consider an observation  $z$  of  $\mathbb{R}^{2L+1}$  that comes from the set of the  $2L + 1$  images of (1) at a given position  $(x, y)$ .

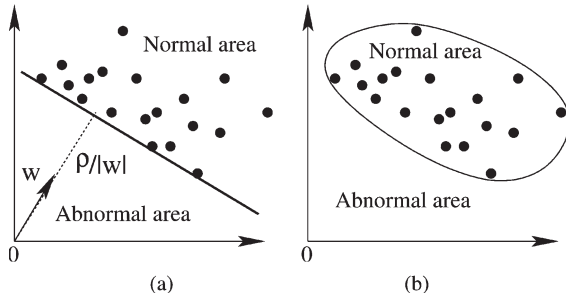


Fig. 2. Separable dataset. (a) With the unique supporting hyperplane separating data from the origin with maximum margin. (b) With a nonlinear characterization.

For oil-slick detection, with the classical formulation of the detection theory, this observation may correspond to hypothesis  $\mathcal{H}_{\text{sea}}$  (i.e., that corresponds to normal sea state) or  $\mathcal{H}_{\text{other}}$  (i.e., that corresponds to an unexpected sea state—to be associated to a slick under some conditions, as shown in Section IV-B).

Many studies have been proposed to draw a theoretical framework for hypothesis testing (from the common formulations of Bayes, minimax, and Neymann–Pearson to the so-called RX or generalized likelihood ratio) [28], [29]. Unfortunately, all those techniques are based on a parametric formulation. Normal sea surface could be modeled through some parametric law, autoregressive methods [8], or a fractal behavior [30]. This required a large amount of data for parameter estimation that may not be available for oil-spill characterization.

Hence, it is proposed to use a nonparametric technique to solve this hypothesis problem. A general solution consists in building a decision function  $f(\cdot)$ , where  $\mathcal{H}_{\text{sea}}$  is decided if  $f(z) > 0$

$$f(z) \begin{cases} \geq 0 & \mathcal{H}_{\text{sea}} \\ < 0 & \mathcal{H}_{\text{other}} \end{cases} \quad (3)$$

Kernel expansion has been chosen to draw this decision function since this technique does not require the knowledge of the statistical model and remains computationally efficient. This technique is known as support vector novelty detection [31].

From a geometric point of view, as shown in Fig. 2(a), the decision function should return a “+1” when applied to the training set  $\{s_1, s_2, \dots, s_m\}$  that corresponds to  $\mathcal{H}_{\text{sea}}$ . The decision function should return a “−1” elsewhere. The strategy is to map the data into  $\mathbb{R}^{2L+1}$  and to separate them from the origin with a maximum margin. For a new observation  $z$ , the value  $f(z)$  is determined by evaluating which side of the hyperplane it falls on. The hyperplane that separates the space in two sides is defined by

$$\begin{aligned} g(z) &= \langle z, w \rangle - \rho \\ &= \sum_{i=1}^m \alpha_i \langle z, s_i \rangle - \rho \end{aligned} \quad (4)$$

where  $w$  is the normal vector of the hyperplane, which depends on the support vectors  $\{s_i\}_{i=1, \dots, m}$  through some linear combi-

nation of dot products  $\langle \cdot, \cdot \rangle$ . Then, the decision function is given by the sign of  $g(\cdot)$

$$f(z) = \text{sgn}(\langle z, w \rangle - \rho). \quad (5)$$

If the training set  $\{s_1, s_2, \dots, s_m\}$  is separable, then there exists a unique supporting hyperplane with the following properties.

- 1) It separates all the data from the origin.
- 2) Its distance to the origin is maximal among all the hyperplanes that fit property 1).

The supporting hyperplane is the one that maximizes the distance to the origin, while each training sample  $s_i$  are located on the same side of the hyperplane with  $f(s_i) > 0$ . The distance to be maximized from the hyperplane to the origin is given by  $\rho/\|w\|$ , so that it yields the following quadratic problem:

$$\text{minimize}_w \frac{1}{2} \|w\|^2 \quad \text{subject to} \quad \langle w, s_i \rangle \geq \rho, \quad \forall i \in \{1, 2, \dots, m\}.$$

In fact, we do not use directly the observations from (1) since there is no reason for the distance to the origin of the space  $\mathbb{R}^{2L+1}$  to be relevant for hypothesis  $\mathcal{H}_{\text{sea}}$  with no false alarms. That is why a feature space is defined to add a thematic point of view to the anomaly detection.

### B. Kernel Design for Slick Detection

Let  $\Phi(\cdot)$  be the feature map that transforms initial observations in  $\mathbb{R}^{2L+1}$ , which come from (1), into a feature space where oil-slick signatures are becoming highly contrasted. The initial dot product is transformed into a kernel evaluation

$$K(z, z') = \langle \Phi(z), \Phi(z') \rangle.$$

Then, the normal vector becomes  $w = \sum_i \alpha_i \Phi(s_i)$  in the feature space, and the hyperplane, which performs linear separation, becomes

$$f(z) = \sum_{i=1}^m \alpha_i K(s_i, z) - \rho \quad (6)$$

which is given by the dual problem:

$$\begin{aligned} \text{minimize}_w \quad & \frac{1}{2} \sum_{i,j \in \{1, \dots, m\}} \alpha_i \alpha_j K(s_i, s_j) \\ \text{subject to} \quad & 0 \leq \alpha_i \leq \frac{1}{\nu m} \quad \text{and} \quad \sum_{i=1}^m \alpha_i = 1. \end{aligned} \quad (7)$$

Here,  $\nu \in ]0, 1]$  is introduced in close analogy to the  $\nu$ -SV classification algorithm [32]. If  $\nu$  tends to approach to zero, the upper bounds on the Lagrange multipliers tend to approach infinity, and the constraint of (7) vanishes. We are facing a hard margin problem.

The kernels are relevant to the behavior of the dot product into the feature space. Kernels to be used for oil-slick detection have to locate slick observations near the origin, while normal sea state can be located far away. We remind that oil slick is characterized by: 1) a lack of radiometry and 2) a damping of the wave spectrum. The use of the wavelet transform transfers

these physical properties into numerical properties: the wavelet coefficients tend to be lowered inside a slick.

1) *Usual Kernels*: For the oil-slick segmentation, we observed that polynomial (8) or sigmoid kernels (9) were the more satisfactory since they minimize the number of false alarms:

$$K_{\text{Polynomial}}(\mathbf{z}, \mathbf{s}_i) = (\langle \mathbf{z}, \mathbf{s}_i \rangle + 1)^P \quad (8)$$

$$K_{\text{Sigmoid}}(\mathbf{z}, \mathbf{s}_i) = \tanh(\langle \mathbf{z}, \mathbf{s}_i \rangle + 1). \quad (9)$$

Those kernels are based on the classical dot product, and  $\mathbf{z}$  tends to approach to zero into the slicks ( $\mathbf{0} \in \mathbb{R}^{2L+1}$ , i.e., a lower radiometry and surface roughness), as shown in Fig. 2.

2) *Texture Kernels*: It is of interest to consider not only pointwise observations through vector-to-vector comparisons but also local neighborhoods to perform the local characterization of the sea-surface wave spectra. A texture-based kernel has been developed in order to act as a contrast measure of local texture on each component of the vectors.

Let us consider the neighborhood of each component of vectors  $\mathbf{z}$  and  $\mathbf{z}'$ . Here, each component  $\{z_1, z_2, \dots, z_{2L+1}\}$  of  $\mathbf{z}$  are wavelet coefficients according to (1). Furthermore, the neighborhood concept is to be understood as a spatial neighborhood on the image (on the sea surface) and not through a Euclidean distance into the feature space.

For the accuracy of the local parameter estimation, local probability density functions (pdfs) have been chosen to follow the Gaussian law that is supposed to be independent from a component to another. Distributions are compared through the Bhattacharyya distance  $[\mathcal{B}(\cdot, \cdot)]$ .

Thus, the texture kernel may be defined, as an RBF kernel, as

$$K(\mathbf{z}, \mathbf{z}') = e^{-(1-\mathcal{B}(p_{\mathbf{z}}, p_{\mathbf{z}'}))}$$

$$\text{with } \mathcal{B}(p_{\mathbf{z}}, p_{\mathbf{z}'}) = \prod_{\ell=0}^{L-1} \int \sqrt{p_{z_\ell}(u)p_{z'_\ell}(u)} du. \quad (10)$$

Since  $\mathcal{B}(p_{\mathbf{z}}, p_{\mathbf{z}'}) \in [0, 1]$ , the kernel of (10) satisfies Mercer's conditions.

3) *Mixture of Kernels*: It is of interest to consider not only the backscattering process but also its local shape. A linear mixture of kernels can fit the dual point of view: similarity according to the dot product and also similarity according to the texture. A mixture of kernels may be defined as [33]

$$K(\mathbf{z}, \mathbf{z}') = \mu K_a(\mathbf{z}, \mathbf{z}') + (1 - \mu) K_b(\mathbf{z}, \mathbf{z}') \quad (11)$$

where  $K_a(\cdot, \cdot)$  and  $K_b(\cdot, \cdot)$  are two kernels. Since  $K_a(\cdot, \cdot)$  and  $K_b(\cdot, \cdot)$  satisfy Mercer's conditions, all linear combinations are eligible for kernels.

## V. APPLICATIONS

Let us summarize the procedure for oil-slick detection.

- 1) SAR image  $I$  is composed of a multiscale representation that yields a vector with  $2L + 1$  components:  $(I_L^{\text{low}}, WI_{L-1}^x, WI_{L-1}^y, \dots, WI_0^x, WI_0^y)^t$ , according to (1).
- 2) A region of interest (ROI) is defined from a nonpolluted sea area to the kernel design of (7). The choice of the ROI for a kernel-based anomaly-detection design is not as

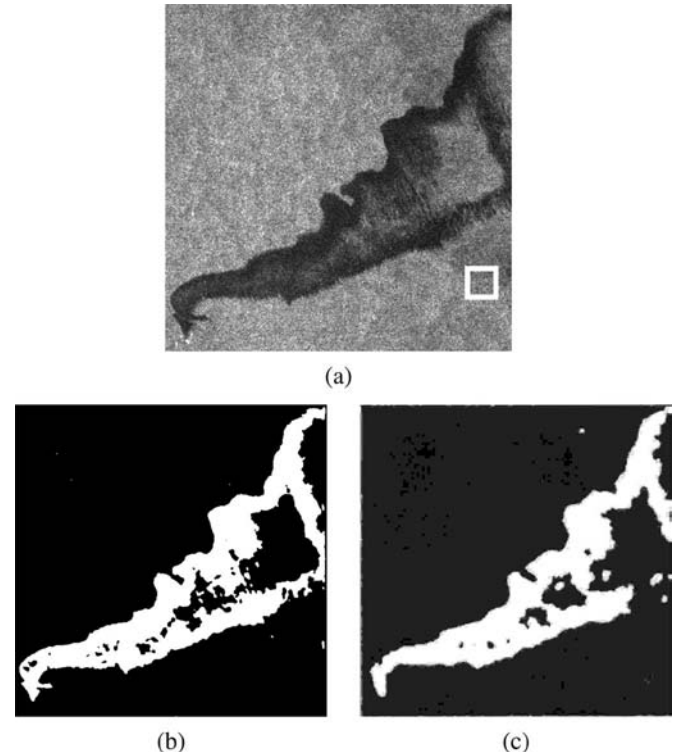


Fig. 3. Detection results on a study area extracted from an ENVISAT ASAR image, November 17, 2002 (10h45 UTC, orbit 3741, pol VV, wide swath mode, and pixel size  $75 \times 75$  m). (a) Initial image with the ROI (white square) used to define the decision function (3550 pixels). (b) Detection results with our method. (c) Detection results with the JRC algorithm. Note the presence of boats near the tanker at the bottom left of the image. Image courtesy of ESA.

crucial as in the case of a maximum-likelihood approach. Nevertheless, it is recommended to define a training set that will improve the difference between the ambiguous area and the polluted area. In the following examples, training sets were defined through ROI of approximately 2000 pixels.

- 3) The overall classification is performed by the sign of the kernel expansion of (6). The computational cost of the classification depends on the complexity of (6). It takes a minute (on a 1.8-GHz Linux Laptop) to classify a  $512 \times 512$  image, including the wavelet transform procedure. The training procedure (7) takes 10 s or so.

### A. Accident Monitoring

A typical example that was chosen occurred during the Prestige wreck in November 2002 near the Spanish coast. An ENVISAT ASAR image was acquired on November 17, which is four days after the accident and two days before it sunk. A complete analysis of this case with synergistic data may be found in [16]. Wreckage can be seen as strong backscatters on the bottom left of the extracted image in Fig. 3(a). The slick by itself is easy to detect (since meteorological conditions, which are shown by QuikSCAT SeaWinds observations, proved there is enough wind speed—from 7 to  $10 \text{ m} \cdot \text{s}^{-1}$ —to exclude a detection of a natural film). Nevertheless, some dark areas (due to atmospheric perturbation [16]) often induce false alarms.

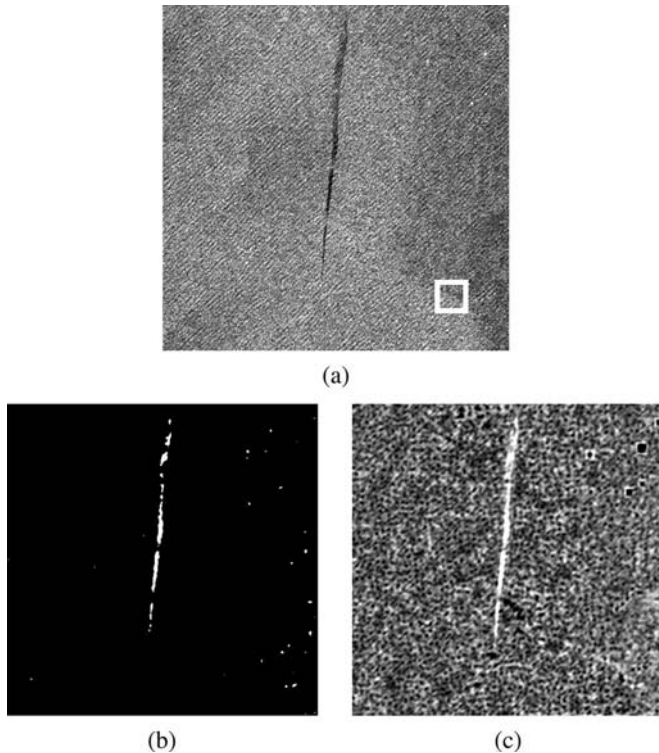


Fig. 4. Detection results on a study area extracted from an ENVISAT ASAR image, January 6, 2003 (22h30 UTC, orbit 4464, pol VV, wide swath mode, and pixel size  $75 \times 75$  m). (a) Initial image with the ROI used to define the decision function (6308 pixels). (b) Detection results. (c) Distance to hyperplane. Image courtesy of ESA.

Before applying any slick-detection algorithm, the backscatter image is calibrated and transformed into a sea-surface roughness image using an ocean backscatter model such as the C-band model (CMOD), as described in [34]. This important step removes the incidence angle dependence across the range and thus enables estimation of global statistics on the sea-surface image that are used in most detection algorithms.

Kernel expansion was trained in a small area, delimited by the white square in Fig. 3(a). A decision of (3) has been applied, and it yields the results shown in Fig. 3(b). It is of interest to stress that strong backscatters (such as boats near the tanker) do not interfere into the slick-detection accuracy. The Joint Research Centre (JRC) algorithm has been chosen for comparison since this algorithm is used routinely for detecting pollution over the Mediterranean Sea [35]. The result [Fig. 3(c)] is very close to our detection [Fig. 3(b)]. This first example shows that kernel-based slick detection yields similar results as the classical methods on an easy case.

### B. Oil Dumping Detection

Another example has been selected from an ENVISAT ASAR acquisition of the same area (south of Galicia), but not connected to the Prestige's wreck. This image [Fig. 4(a)], acquired on January 6, 2003, shows a 30-km-long thin linear oil spill, but the wind speed (which has been estimated to be up to  $5\text{--}12 \text{ m} \cdot \text{s}^{-1}$  from the SAR image itself [34] and also from QuikSCAT SeaWinds observations) is strong enough to ensure spill detection. This case is interesting since the linear

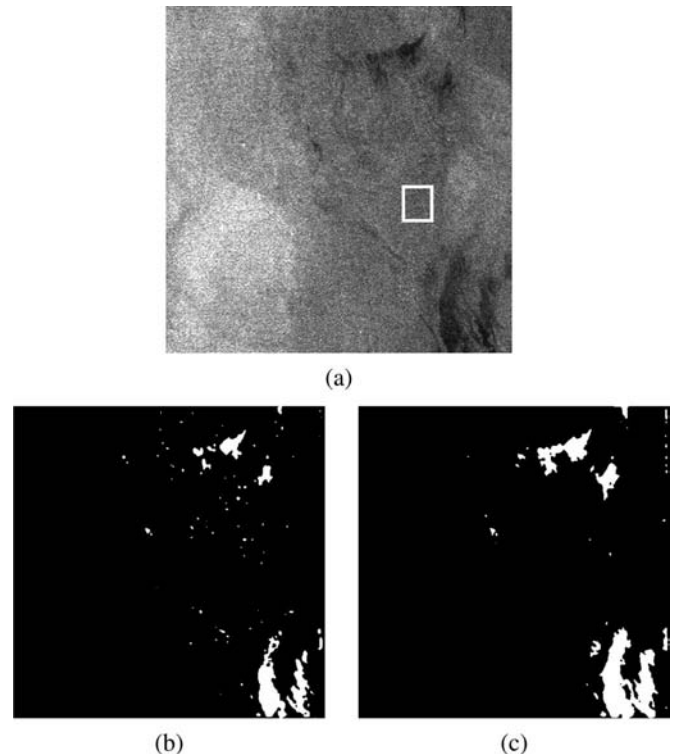


Fig. 5. Detection results on a study area extracted from an ENVISAT ASAR image, December 2, 2002 (22h30 UTC, orbit 3963, pol VV, wide swath mode, and pixel size  $75 \times 75$  m). (a) Initial image with the ROI used to define the decision function (1665 pixels). (b) Detection results. (c) Detection result by using the decision function built in Fig. 4. Image courtesy of ESA.

oil spill is easy to detect by eyes, but most of the automatic detections fail. It is mostly due to swell, which is dominant in the background of the slick and which induces noncontiguous detections (the significant wave height is estimated to be 5 m with the Wave Watch III model [36]).

The 6308-pixel ROI includes a dark area induced by atmospheric conditions. The spill detection still shows false alarms, but the detection itself remains accurate [Fig. 4(b)]. Also, a distance map to the hyperplane [values of (6) shown in Fig. 4(c)] can be used to connect the linear spill. Moreover, the distance map shows that ships [that appear dark in Fig. 4(c)] are located to the opposite side of the feature space from the spill. It confirms the good choice of the kernel. In comparison, the JRC algorithm used, in this case does not detect this particular linear spill.

While the proposed technique yields similar results on the first case (which may be considered as a toy case), the kernel expansion proved to be interesting when classical methods failed.

### C. Ambiguous Area

During the weeks following the Prestige tanker accident, SAR images were acquired in order to monitor the oil-spill drift. The image for December 2 was acquired in this context. It was an example of complex detection because of the weak contrast of the dark patches, which could be oil spills or not [Fig. 5(a) shows an extracted area]. The detailed synergistic data analysis for this case is available in [16]. This day was characterized by strong north-northwesterly winds higher than

10 m · s<sup>-1</sup>. This direction implies that dark patches do not correspond to weak winds due to an orographic effect. Moreover, the swell of the same direction has a 3–4-m significant wave height. These conditions imply that the dark patches detected in the SAR image are probably not due to natural phenomena but are thick oil spills drifting on the ocean surface. This conclusion is confirmed by aircraft observation maps [16]. Fig. 5(b) shows the detection of oil slicks from kernel-based detection. Although the JRC algorithm does not detect any slick on this difficult scene, kernel-based detection shows interesting patches that correspond to real slicks. Unfortunately, no real ground truth is available, so that it is not possible to draw receiver operating characteristics (ROC) curves to evaluate the ratio between good detection and the number of false alarms that are surely found here.

In order to show the ability of stochastic kernels to learn a normal sea state and to generalize normal conditions, this ambiguous case has been processed by using the decision function of (6), which is trained from the previous image [Fig. 4(a)]. The result, shown in Fig. 5(c), proves that the learning of normal sea state may be used for the complete image (and not only from a selected area) and, also, for a set of images associated to equivalent meteo-oceanic conditions.

## VI. CONCLUSION

SAR imagery is well adapted to detect ocean pollution independently from daily or weather conditions. Detection may be performed on operational conditions when the impacts of a viscous slick on the sea surface and then on the SAR data are carefully taken into consideration. In this paper, a semisupervised oil-slick detection technique is proposed by using single-class support vector machines into a wavelet decomposition of a SAR image. A specific kernel is developed to perform accurate segmentation of the local sea-surface wave spectrum by using both radiometric and texture information. Instead of the previous studies such as in [37] and [38], this technique is efficient in an operational context and proves to be a relevant strategy to detect oil slicks as abnormal situations of the sea-surface roughness and radiometry.

The proposed technique is as follows:

- 1) fast and can be applied on large images;
- 2) efficient since the detection is equivalent or better than classical tools;
- 3) able to be generalized and made generic by using precalculated kernels.

Actually, deeper validation has to be made by considering the synergistic data derived from the data of SAR itself (for wind only) or any other sensor. To perform an accurate detection and to reduce human supervision, it is of interest now to consider a kernel family that can integrate such meteo-oceanic information. It may significantly reduce false alarms from classical look alike.

## ACKNOWLEDGMENT

The authors would like to thank the European Space Agency for the ENVISAT ASAR images and the National Oceanic and Atmospheric Administration for the Wave Watch III model.

## REFERENCES

- [1] T. Elfouhaily and B. Chapron, "A comparison of wind wave spectra used in ocean remote sensing modeling," in *Proc. IGARSS*, Lincoln, NE, May 27–31, 1996, vol. 1, pp. 606–608.
- [2] M. Gade, W. Alpers, H. Hühnerfuss, V. Wismann, and P. Lange, "On the reduction of the radar backscatter by oceanic surface films: Scatterometer measurements and their theoretical interpretation," *Remote Sens. Environ.*, vol. 66, no. 1, pp. 52–70, Oct. 1998.
- [3] M. Gade, J. Scholz, and C. von Viebahn, "On the detectability of marine oil pollution in European marginal waters by means of ERS SAR imagery," in *Proc. IGARSS*, Honolulu, HI, Jul. 24–28, 2000, vol. 6, pp. 2510–2512.
- [4] P. Lombardo, D. Conte, and A. Morelli, "Comparison of optimised processors for the detection and segmentation of oil slicks with polarimetric SAR images," in *Proc. IGARSS*, Honolulu, HI, Jul. 24–28, 2000, vol. 7, pp. 2963–2965.
- [5] K. W. Bjerde, A. H. S. Solberg, and R. Solberg, "Oil spill detection in SAR imagery," in *Proc. IGARSS*, Tokyo, Japan, Aug. 18–21, 1993, vol. 3, pp. 943–945.
- [6] A. H. S. Solberg, G. Storvik, R. Solberg, and E. Volden, "Automatic detection of oil spills in ERS SAR images," *IEEE Trans. Geosci. Remote Sens.*, vol. 37, no. 4, pp. 1916–1924, Jul. 1999.
- [7] H. Espedal, "Detection of oil spill and natural film in the marine environment by spaceborne SAR," in *Proc. IGARSS*, Hamburg, Germany, Jun. 28–Jul. 2 1999, vol. 3, pp. 1478–1480.
- [8] M. Bertacca, F. Berizzi, and E. D. Mese, "A FARIMA-based technique for oil slick and low-wind areas discrimination in sea SAR imagery," *IEEE Trans. Geosci. Remote Sens.*, vol. 43, no. 11, pp. 2484–2493, Nov. 2005.
- [9] B. Franklin, "Of the stilling of waves by means of oil," *Philos. Trans.*, vol. 64, pt. 1, pp. 445–460, 1774.
- [10] C. Marangoni, "Sul principio della viscosità superficiale dei liquidi stabilito dal Sig. J. Plateau," *Nuovo Cim.*, ser. 2, vol. 5/6, pp. 239–273, 1872.
- [11] W. Alpers and H. Hühnerfuss, "Radar signatures of oil films floating on the sea surface and the Marangoni effect," *J. Geophys. Res.*, vol. 93, no. C4, pp. 3642–3648, 1988.
- [12] —, "The damping of ocean waves by surface films: A new look at an old problem," *J. Geophys. Res.*, vol. 94, no. C5, pp. 6251–6265, 1989.
- [13] W. Hühnerfuss, W. Alpers, and W. L. Jones, "Measurements at 13.9 GHz of the radar backscattering cross section of the North Sea covered with an artificial surface film," *Radio Sci.*, vol. 13, no. 6, pp. 979–983, 1978.
- [14] W. Hühnerfuss, W. Alpers, A. Cross, W. D. Garrett, W. C. Keller, P. A. Lange, W. J. Plant, F. Schlude, and D. L. Schuler, "The modification of X and L-band radar signals by monomolecular sea slicks," *J. Geophys. Res.*, vol. 88, no. C14, pp. 9817–9822, 1983.
- [15] H. Hühnerfuss, W. Alpers, W. D. Garrett, P. A. Lange, and S. Stolte, "Attenuation of capillary and gravity waves at sea by monomolecular organic surface films," *J. Geophys. Res.*, vol. 88, no. C14, pp. 9809–9816, 1983.
- [16] F. Girard-Ardhuin, G. Mercier, F. Collard, and R. Garello, "Operational oil slick characterization by SAR imagery and synergistic data," *IEEE J. Ocean. Eng.*, vol. 30, no. 3, pp. 487–495, Jul. 2005.
- [17] V. Wismann, "Radar signatures of mineral oil spills measured by an airborne multi-frequency radar and the ERS-1 SAR," in *Proc. IGARSS*, Tokyo, Japan, Aug. 18–21, 1993, pp. 940–942.
- [18] P. Pavlakis, A. Sieber, and S. Alexandry, "On the optimization of spaceborne SAR capacity in oil spill detection and the related hydrodynamic phenomena," *Spill Sci. Technol. Bull.*, vol. 3, no. 1/2, pp. 33–40, 1996.
- [19] M. Gade, W. Alpers, H. Hühnerfuss, H. Masuko, and T. Kobayashi, "Imaging of biogenic and anthropogenic ocean surface films by the multifrequency/multipolarization SIR-C/X-SAR," *J. Geophys. Res.*, vol. 103, no. C9, pp. 18851–18866, 1998.
- [20] G. Franceschetti, A. Iodice, D. Riccio, G. Ruello, and R. Siviore, "SAR raw signal simulation of oil slicks in ocean environments," *IEEE Trans. Geosci. Remote Sens.*, vol. 40, no. 9, pp. 1935–1949, Sep. 2002.
- [21] V. Wismann, M. Gade, W. Alpers, and H. Hühnerfuss, "Radar signatures of marine mineral oil spills measured by an airborne multi-frequency radar," *Int. J. Remote Sens.*, vol. 19, no. 18, pp. 3607–3623, 1998.
- [22] K. P. Singh, A. L. Gray, R. K. Hawkins, and R. A. O'Neil, "The influence of surface oil on C- and Ku-band ocean backscatter," *IEEE Trans. Geosci. Remote Sens.*, vol. GRS-24, no. 5, pp. 738–744, Sep. 1986.
- [23] H. Masuko, T. Kobayashi, K. Okamoto, and W. Alpers, "Observation of artificial slicks with SIR-C/X-SAR around Japan," in *Proc. IGARSS*, Florence, Italy, Jul. 10–14, 1995, vol. 1, pp. 227–229.
- [24] I. Daubechies, *Ten Lectures on Wavelets*. Philadelphia, PA: SIAM, 1992.

- [25] S. Mallat and S. Zhong, "Characterization of signals from multiscale edges," *IEEE Trans. Pattern Anal. Mach. Intell.*, vol. 14, no. 7, pp. 710–732, Jul. 1992.
- [26] C. Kiecy and C. Lennard, "Unique reconstruction of band-limited signals by a Mallat–Zhong wavelet transform algorithm," *Fourier Anal. Appl.*, vol. 3, no. 1, pp. 63–82, 1997.
- [27] S. Mallat, *A Wavelet Tour of Signal Processing*. New York: Academic, 1998.
- [28] H. V. Poor, *An Introduction to Signal Detection and Estimation*, 2nd ed. New York: Springer-Verlag, 1994.
- [29] I. S. Reed and X. Yu, "Adaptive multiple-band CFAR detection of an optical pattern with unknown spectral distribution," *IEEE Trans. Acoust., Speech, Signal Process.*, vol. 38, no. 10, pp. 1760–1770, Oct. 1990.
- [30] F. Berizzi and E. D. Mese, "Scattering coefficient evaluation from a two-dimensional sea fractal surface," *IEEE Trans. Antennas Propag.*, vol. 50, no. 4, pp. 426–434, Apr. 2002.
- [31] J. Kivinen, A. J. Smola, and R. C. Williamson, "Online learning with kernels," *IEEE Trans. Acoust., Speech, Signal Process.*, vol. 52, no. 8, pp. 2165–2176, Aug. 2004.
- [32] V. N. Vapnick, *Statistical Learning Theory*. New York: Wiley, 1998.
- [33] G. Smits and E. Jordaen, "Improved SVM regression using mixtures of kernels," in *Proc. Int. Joint Conf. Neural Netw.*, May 12–17, 2002, vol. 3, pp. 2785–2790.
- [34] Y. Quilfen, B. Chapron, T. Elfouhaily, K. Katsaros, and J. Tourmadre, "Observation of tropical cyclones by high resolution scatterometry," *J. Geophys. Res.*, vol. 103, no. C4, pp. 7767–7786, 1998.
- [35] P. Pavlakis, A. J. Sieber, and S. Alexandry, "Monitoring oil-spill pollution in the Mediterranean with ERS SAR," *Earth Obs. Q.*, vol. 52, no. 4, pp. 13–16, 1994.
- [36] H. L. Tolman, *Validation of WAVEWATCH III Version 1.15 for a Global Domain*, 2002. NOAA/NWS/NCEP/OMB, Tech. Note 213. [Online]. Available: <http://polar.ncep.noaa.gov/waves/references.html>
- [37] G. Mercier, S. Derrode, W. Pieczynski, J.-M. Le Caillec, and R. Garello, "Multiscale oil slick segmentation with Markov chain model," in *Proc. IGARSS*, Toulouse, France, Jul. 21–25, 2003, pp. 3501–3503.
- [38] G. Mercier and F. Girard-Ardhuin, "Oil slick detection by SAR imagery using support vector machines," in *Proc. IEEE Oceans—Europe*, Brest, France, Jun. 20–23, 2005, pp. 90–95.



**Grégoire Mercier** (M'02) was born in France, in 1971. He received the engineering degree from the Institut National des Télécommunications (INT), Evry, France, in 1993, and his Ph.D. degree from the University of Rennes I, Rennes, France, in 1999.

Since 1999, he has been with the Ecole Nationale Supérieure des Télécommunications de Bretagne (ENST Bretagne), Brest, France, where he is currently an Associate Professor in the Image and Information Processing Department. His research interests are in remote-sensing image compression and segmentation, especially in hyperspectral and synthetic aperture radar. His research is dedicated especially to change detection and to combat pollution.



**Fanny Girard-Ardhuin** (M'03) was born in 1975. She received the Ph.D. degree in radar meteorology from the Laboratoire d'Aérodynamique, Toulouse, France, in 2001, where her thesis was dedicated to the atmospheric boundary layer study, using wind-profiler radar with a radio acoustic sounding system.

She spent one year with the Ecole Nationale Supérieure des Télécommunications de Bretagne (ENST Bretagne), Brest, France, in 2003, working on synthetic aperture radar (SAR) images for the European project Marine SAR Analysis and Interpretation System (MARS AIS), including oil-spill detection. She joined the Brest Operational Observation Systems and Technologies (BOOST) to test oil-slick-detection algorithms applied on SAR images. She is currently working as a Postdoctoral Research Associate with the Institut Français de Recherche pour l'Exploitation de la MER (IFREMER), where her main research interest lies in sea-ice observation from active and passive satellites.